MBE growth of few-layer 2H-MoTe₂ on 3D substrates

Suresh Vishwanath [a,b,*], Aditya Sundar [c], Xinyu Liu [d], Angelica Azcatl [e], Edward Lochocki [f], Arthur R. Woll [g], Sergei Rouvimov [b], Wan Sik Hwang [b], Ning Lu [e], Xin Peng [e], Huai-Hsun Lien [c], John Weisenberger [b], Stephen McDonnell [e,h], Moon J. Kim [e], Margaret Dobrowolska [d], Jacek K. Furdyna [d], Kyle Shen [f,i], Robert M. Wallace [e], Debdeep Jena [a,b,c], Huili Grace Xing [a,b,c,i]

[a] School of Electrical and Computer Engineering, Cornell University, Ithaca, NY 14853, United States
[b] Department of Electrical Engineering, University of Notre Dame, IN 46556, United States
[c] Department of Materials Science and Engineering, Cornell University, Ithaca, NY 14853, United States
[d] Department of Physics, University of Notre Dame, Notre Dame, IN 46556, United States
[e] Department of Materials Science and Engineering, University of Texas Dallas, Dallas, TX 75083, United States
[f] Department of Physics, Laboratory of Atomic and Solid State Physics, Cornell University, Ithaca, NY 14853, United States
[g] Cornell High Energy Synchrotron Source, Cornell University, Ithaca, NY 14853, United States
[h] Department of Materials Science and Engineering, University of Virginia, Charlottesville, VA 22904, United States
[i] Kavli Institute at Cornell for Nanoscale Science, Cornell University, Ithaca, NY 14853, United States

ARTICLE INFO

ABSTRACT

MoTe₂ is the least explored material in the Molybdenum-chalcogen family. Molecular beam epitaxy (MBE) provides a unique opportunity to tackle the small electronegativity difference between Mo and Te while growing layer by layer away from thermodynamic equilibrium. We find that for a few-layer MoTe₂ grown at a moderate rate of ∼6 min per monolayer, a narrow window in temperature (above Te cell temperature) and Te:Mo ratio exists, where we can obtain pure phase 2H-MoTe₂. This is confirmed using reflection high-energy electron diffraction (RHEED), Raman spectroscopy and X-ray photoemission spectroscopy (XPS). For growth on CaF₂, Grazing incidence X-ray diffraction (GI-XRD) reveals a grain size of ∼90 Å and presence of twinned grains. In this work, we hypothesis the presence of excess Te incorporation in MBE grown few layer 2H-MoTe₂. For film on CaF₂, it is based on >2 Te:Mo stoichiometry using XPS as well as 'a' and 'c' lattice spacing greater than bulk 2H-MoTe₂. On GaAs, its based on observations of Te crystallite formation on film surface, 2×2 superstructure observed in RHEED and low energy electron diffraction, larger than bulk c-lattice spacing as well as the lack of electrical conductivity modulation by field effect. Finally, thermal stability and air sensitivity of MBE 2H-MoTe₂ is investigated by temperature dependent XRD and XPS, respectively.

1. Introduction

MoTe₂ is still a relatively unexplored transitional metal dichalcogenide (TMD) and holds great promise. MoTe₂ exists in trigonal prismatic (2H structure) semiconducting phase at room temperature and metallic 1T' phase (monoclinic structure) at high temperatures or metallic T_d phase (orthorhombic structure) when metastable 1T' is cooled to −33 °C to −13 °C [1]. 1T' and T_d crystals have the same in-plane crystal structures but vary in vertical stacking. Monolayer 2H-MoTe₂ is predicted to be among the smallest bandgap semiconducting TMDs [2]. Using scanning tunneling spectroscopy (STS) measurements, the bandgap of monolayer 2H-MoTe₂ has been measured to be between 1.03 eV [3] to 1.4 eV [4]. 2H-MoTe₂ has a close to broken band alignment with materials like SnSe₂ [5], making them attractive for tunnel based devices such as Esaki diodes [6] and two-dimensional heterojunction interlayer tunneling field effect transistors (Thin-TFETs) [7,8]. The T_d-MoTe₂ is a type II Weyl semimetal [1], which is a new class of topological material. Traditionally, the transition between 2H and 1T' phase was thought to be abrupt with respect to temperature [9] but recently a mixed phase region has been observed in the phase diagram [10]. Even for growth under UHV conditions, coexistence of 2H and 1T' phase has been recently reported [11]. The transition between the 2H and 1T' phase holds promise for applications such as low resistance contacts [12] and phase change memory.

* Corresponding author at: School of Electrical and Computer Engineering, Cornell University, Ithaca, NY 14853, United States.
E-mail addresses: sv372@cornell.edu (S. Vishwanath), grace.xing@cornell.edu (H.G. Xing).

Large area, phase-pure epitaxial growth with layer controllability would enable industrial applications, but growth of MoTe$_2$ is especially challenging, since the electronegativity difference between Mo and Te is just 0.3 eV [13–15], resulting in a weak bond. Until recently, MoTe$_2$ has been obtained using tellurization of e-beam deposited molybdenum or molybdenum oxide films [16–18] or by chemical vapor transport (CVT) [19,10]. In case of tellurizing Mo, 1T'-MoTe$_2$ phase is initially formed at 650 °C, which can be converted to 2H-MoTe$_2$ by a 3 h anneal under Te vapor [17]. Tellurizing MoO$_3$ transforms to 2H-MoTe$_2$ more readily, but one cannot be sure in achieving 100% percent reduction of oxygen. For CVT grown MoTe$_2$ a mixed phase is observed in the growth temperature range of 500–900 °C based on the tellurium content in MoTe$_x$ [10], but under ultrahigh vacuum (UHV) in non-thermodynamic equilibrium conditions, this phase boundary is unknown. For example, the formation of a new metallic nanowire phase has been recently reported upon Te loss by annealing at 400-500C in UHV [20]. We recently demonstrated growth of 2H-MoTe$_2$ using molecular beam epitaxy (MBE) in a superlattice with MoSe$_2$ as well as Bi$_2$Te$_3$ [21], where we used a growth temperature of 380 °C. Growth temperature of ~340 °C [22] or 200 °C [3,4] have been used in other recent MBE demonstrations of 2H-MoTe$_2$ growth. Also, work on phase purity and stability for MBE 2H-MoTe$_2$ has been done only on monolayer MoTe$_2$ grown on layered substrates [3,4,11].

In this study, we chose 340 °C to be the lower bound of growth temperature, so as to keep the growth temperature higher than the Te cell temperature (~300 °C). This avoids intentional accumulation of Te, while keeping the growth temperature significantly lower than the lower bound (500 °C) of the mixed phase, as suggested by the phase diagram under 1 ATM of Te vapor [10]. We observe that even at a substrate growth temperature as low as 340 °C, the crystalline phase of the MBE-grown MoTe$_2$ has a sensitive dependence on uncracked Te flux in a Te rich environment (Te: Mo > 70 for all growths). This is presented by analyzing a series of 3 samples of MoTe$_2$ under different growth conditions on CaF$_2$ and identifying a growth condition for growth of pure phase 2H-MoTe$_2$. Here, we show that it is indeed feasible to grow phase-pure 2H-MoTe$_2$ on a CaF$_2$ substrate without any requirement of a post-growth anneal. We also present the growth and electrical characterization of 2H-MoTe$_2$ on GaAs (1 1 1) B. The transition to GaAs was motivated by the availability of high quality epi-ready n$^+$ GaAs substrates necessary for characterization using techniques such as low energy electron diffraction (LEED). Table 1 summarizes the growth conditions of all the 5 samples in this study. The Mo flux is calculated using the experimentally determined growth rates while assuming zero desorption for molybdenum adatoms, which enables calculation of the Te:Mo flux ratio tabulated in Table 1 for all samples. Growth rate on CaF$_2$ is calculated using cross-section transmission electron microscopy image and on GaAs

(1 1 1) B from Reflection high-energy electron diffraction (RHEED) oscillations.

2. Growth conditions

2.1. Growths on CaF$_2$ substrate

Three samples (see Table 1) constitute the series of samples grown on CaF$_2$. Calcium fluoride was chosen as a substrate because (i) it has an inert fluorine-terminated surface on which we have successfully grown MoSe$_2$ [23] and (ii) it provides a cavity effect enhancing the Raman signal due to its optical transparency. On the other hand, the Raman signal from MoTe$_2$ grown on GaAs (1 1 1) B is very weak [21]. These samples were grown in a Riber 32 MBE system using elemental Mo delivered from an e-beam evaporator and elemental uncracked Te from a Knudsen cell. The growth duration was 30 min for each sample and the Mo flux, which limits the growth rate, was set to ~0.17 monolayer (ML) per minute or 6 min per ML. Supplementary (SI) Fig. 1(a) shows that all CaF$_2$ substrates were first heated to 800 °C, held for 30 min in order to anneal and degas. Sharp RHEED streaks of CaF$_2$ prior to start of growth (see Fig. 1(a)), show the smooth crystalline post-anneal growth surface. Then the substrates were lowered to respective growth temperatures, stabilized for ~30 min prior to thin film growth. The growth conditions are listed in Table 1. Using these 3 samples, we observe that, although the Te flux is ~2 orders of magnitude higher than the Mo flux, the Te flux range to obtain 2H-MoTe$_2$ is narrow and the substrate temperature control is critical. None of the MoTe$_2$ films on CaF$_2$ have been annealed in order to avoid phase change during annealing. All temperatures given in this study are thermocouple temperatures and the sample surface temperature is estimated about 20 °C lower than the thermocouple temperature.

All samples on CaF$_2$ where grown on the same day under identically Mo flux conditions. Hence, identical film thickness of ~5ML is expected for the three samples on CaF$_2$. TEM was done on sample A and sample B, discussed further below, to confirm similar film thickness.

2.2. Growths on GaAs substrate

Two samples, sample D and sample E, of MoTe$_2$ on GaAs (1 1 1) B are discussed. Post-growth anneal was done on MoTe$_2$ films on GaAs.

Sample D was grown at a growth temperature of 340 °C and Te flux of 6.9×10^{-6} Torr (slightly higher than Sample A due to higher thermal conductivity of GaAs than CaF$_2$). SI Fig. 1(b), shows the growth sequence. The key step in this growth is the anneal of GaAs under Te prior to MoTe$_2$ growth to achieve smoother Te terminated

Table 1
Growth conditions for all samples in this study.

Sample ID	Substrate	MoTe$_2$ phase	Substrate temperature (°C)	Te flux (Torr)	Te:Mo flux ratio	Growth duration (mins)	Post growth anneal
A	CaF$_2$ (1 1 1)	2H	340	6.5×10^{-6}	297	30	None
B	CaF$_2$ (1 1 1)	2H + UP*	340	2.0×10^{-6}	98	30	None
C	CaF$_2$ (1 1 1)	UP*	400	1.4×10^{-6}	71	30	None
D	GaAs (1 1 1) B	2H	340	6.9×10^{-6}	175	30	at 380 °C for 10 min without Te
E	GaAs (1 1 1) B	2H	340	6.9×10^{-6}	262	20	at 450 °C for 3 min and 550 °C for 7 min under Te

*UP stands for unidentified phase that has some similarity to 1T' but is not identical.

Growths on CaF$_2$

Growth on GaAs

Post Growth- Sample D
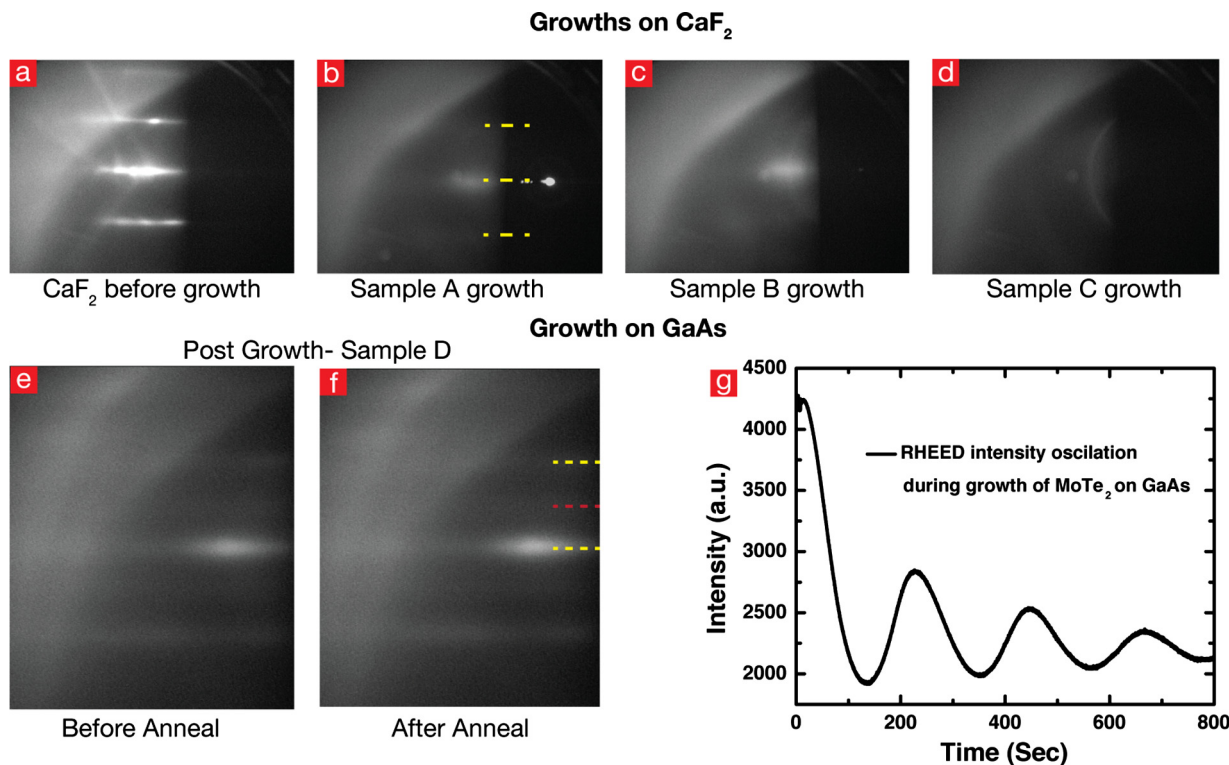
Fig. 1. (a–d) RHEED pattern from the series of samples on CaF$_2$ showing evolution of polycrystalline growth with lowering Te:Mo flux ratio and increasing growth temperature as compared to well-aligned growth of 2H phase. Sample D: RHEED post growth of 2H-MoTe$_2$ on GaAs (e) pre anneal and (f) post anneal are shown. The dashed lines are guide to the eye, yellow for MoTe$_2$ and red for the additional set of lines observed. (g) RHEED oscillations at the spectral point during growth of MoTe$_2$ shows a close to layer by layer growth with a period of ~218 s per monolayer. (For interpretation of the references to colour in this figure legend, the reader is referred to the web version of this article.)

surface. This is consistent with our previous report of Te anneal of GaAs [21] prior to TMD superlattice growth.

Sample E was grown on n$^+$ GaAs for characterizations requiring conducting substrate. Prior to the post-growth anneal, the growth sequence for sample E was identical to sample D. The post-growth anneal for sample E was done at 450 °C for 3 min and 550 °C for 7 min under Tellurium flux. After this post-growth anneal, the sample was cooled under Te till growth temperature of 340 °C and then capped with ~100 nm Se during cool-down to room temperature for surface protection during sample transfer to other characterization tools. The change in growth rate between samples D and E (see Table 1) is due to variability of Mo flux at the same e-beam power on different growth days.

3. Results and discussion

3.1. Reflection high-energy electron diffraction (RHEED)

3.1.1. RHEED on MoTe$_2$ films on CaF$_2$ substrate

As seen in Fig. 1(a), annealed CaF$_2$ has a strong streaky RHEED pattern prior to growth. Sample A shows a more diffused but still streaky RHEED pattern, whereas sample B shows a mixed pattern comprising of streaks and a ring, which evolves into only a ring in sample C. Streaky RHEED points to layered growth with minimal mosaicity of the as-grown film, but progressive inclusion of a ring points to another growth mechanism taking over, which results in polycrystalline growth. Whether the polycrystalline material is the same phase as the streaky film or a different phase is elucidated through employing Raman and XPS characterization (described below). The RHEED streaks of MoTe$_2$ in sample A along $\langle 11\bar{2}0 \rangle$

appear at the same position as the $\langle 1\bar{1}0 \rangle$ of CaF$_2$, as observed previously in MoSe$_2$ on CaF$_2$ [23,24]. The in-plane lattice spacing of MoTe$_2$ based upon the ratio of the RHEED streak spacing is ~3.5 Å, which is very close to the value of 3.52 Å [10] corresponding to bulk 2H-MoTe$_2$. The ambiguity in this measurement is due to the diffused RHEED pattern, which is measured more accurately using grazing incidence X-ray diffraction (GI-XRD), presented further below.

3.1.2. RHEED on MoTe$_2$ films on GaAs substrate

For sample D, a pair of faint RHEED streaks with a spacing less than 2H-MoTe$_2$ were observed. Te has a hexagonal crystal structure with lattice constants of a = 4.456 Å and c = 5.921 Å [25]. Since the inplane lattice constant of Te is greater than that of 2H-MoTe$_2$, it was the initial suspect. With the aim to remove any excess Te in the film, a post-growth anneal at 380 °C without any Te flux was done. But, as seen in Fig. 1(e and f), the anneal doesn't remove this second set of streaks. Further analysis reveals that the ratio of spacing of the RHEED streaks from MoTe$_2$ and the newly observed streaks is ~2. If the lines were from 2H-MoTe$_2$ and Te, the expected ratio is ~1.2. So, its likely not due to elemental tellurium at the surface. One hypothesis is presence of ordered defects, which could be Te interstitials. Fig. 1(g) shows RHEED intensity oscillations of the RHEED spectral point during the growth of MBE 2H-MoTe$_2$. This shows close to layer by layer growth. Simulation in SI Fig. 2 shows the crest and the trough do not necessarily indicate a complete monolayer, variation in smoothness can cause shifts. But approximately, the period between crests corresponds to a monolayer. Increasing roughness or waviness in the film is the likely cause for decay with RHEED oscillation intensity in Fig. 1(g).
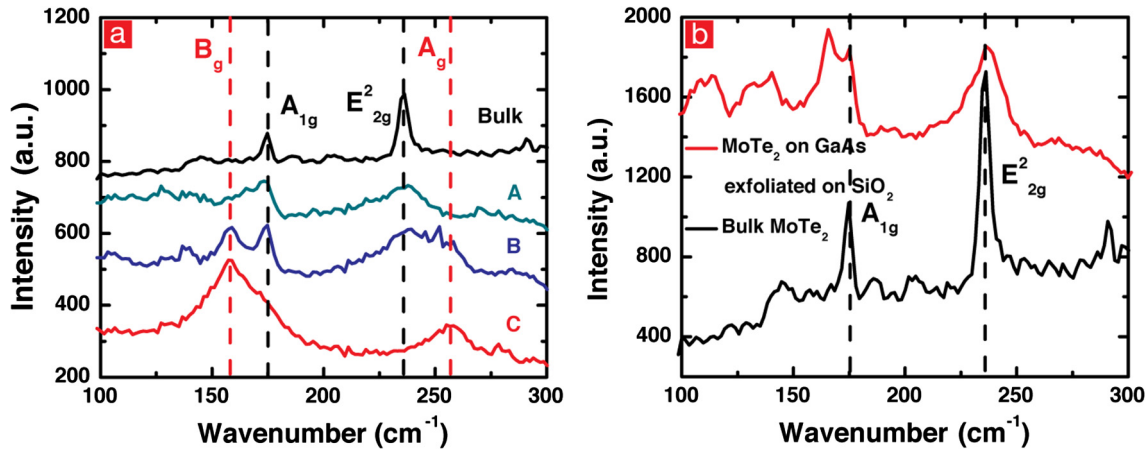
Fig. 2. (a) Raman measurements on the samples grown on CaF$_2$. (b) Raman from MoTe$_2$ grown on GaAs post-exfoliation, using scotch tape, on to SiO$_2$/Si for a better signal.

Table 2
Positions of the various Raman peaks compared to measured values for bulk 2H-MoTe$_2$ and reported values for 1T'-MoTe$_2$ [17].

Sample ID	A$_{1g}$ position (cm^{-1})	E$^2_{2g}$ position (cm^{-1})	B$_g$ position (cm^{-1})	A$_g$ position (cm^{-1})
Bulk 2H	174	236	NA	NA
A	173	236	NA	NA
B	174	237	158	256
C	NA	NA	159	256
1T' [17]	NA	NA	163	256.1

3.2. Raman spectroscopy

3.2.1. Raman on MoTe$_2$ films on CaF$_2$ substrate

Raman spectra in Fig. 2(a) confirm an evolution from the 2H phase to a new phase as we progress from sample A to sample C. The 2H phase is confirmed by comparing Raman from sample A with Raman from CVT grown bulk 2H-MoTe$_2$ obtained from 2D Semiconductors Inc. as shown in Table 2. Its important to note that the FWHM of the peaks from MBE grown MoTe$_2$ is several times wider than that of the CVT-grown MoTe$_2$. This points to a significant disorder in the MBE-grown material and augments the observation of the diffuse MoTe$_2$ RHEED pattern in sample A. The new phase is labeled as the unidentified phase (UP) MoTe$_x$ in this work. This is because, as seen in Table 2 the A$_g$ peak position of the UP phase at ~256 cm^{-1} agrees closely with the reported value of 256.1–257 cm^{-1} for 1T' MoTe$_2$ growth by tellurization of molybdenum films but the peak at 158–159 cm^{-1} deviates significantly from the reported value of 163–161 cm^{-1} for B$_g$ peak from 1T' MoTe$_2$ and is extremely broad [17]16. Sample B shows a mixed phase comprised of Raman signatures from both 2H and UP phases. Sample C is comprised mostly of UP phase but due to the broad peaks, presence of some 2H phase MoTe$_2$ cannot be ruled out.

#### 3.2.2. Raman on MoTe$_2$ films on GaAs substrate

Since, the Raman signal from MoTe$_2$ on GaAs is quite weak [21], the as grown film was exfoliated and transferred to SiO$_2$/Si substrate using a scotch tape. The transfer was performed to enhance the raman signal from the MoTe$_2$ due to cavity effect from SiO$_2$ as well as to eliminate the interference from the LO phonon raman peaks from GaAs. In Fig. 2(b), the peaks below 150 cm^{-1} can be attributed to Te [26]. E$_{2g}$ peak from transferred MoTe$_2$ from sample D is almost symmetric and peak position is consistent with that from bulk MoTe$_2$ at 235.8 cm^{-1}. The reason for broadening in the A$_{1g}$ peak is unclear.

3.3. X-ray photoemission spectroscopy (XPS)

3.3.1. XPS on MoTe$_2$ films on CaF$_2$ substrate

XPS spectra corresponding to Mo, Te, O, Ca, F and C are detected from all samples (Fig. 3). No charging effects were detected on any of them. Peak positions for Mo 3d$_{5/2}$ and Te 3d$_{5/2}$ as well as Te:Mo ratio corresponding to both phases 2H-MoTe$_2$ and UP-MoTe$_x$ are listed in Table 3. For sample A, the Mo 3d$_{5/2}$ signal corresponding to 2H-MoTe$_2$ bond was detected at 227.9 eV, which is consistent with the binding energy of 2H-MoTe$_2$ in literature [14]. The Te 3d$_{5/2}$ peak corresponding to the 2H-MoTe$_2$ is observed at 572.8 eV. Molybdenum oxide in the Mo^{+6} state was also identified. In the Te 3d spectrum, tellurium dioxide and MoTe$_2$ are both detected. The Te:Mo ratio is ~2.57 after correction due to attenuation from the oxide overlayer. For sample B, in addition to the peaks corresponding to 2H-MoTe$_2$, Mo^{+6} oxide and TeO$_2$ are detected; the Mo 3d$_{5/2}$ peak at 227.6 eV and the Te 3d$_{5/2}$ peak at 572.6 eV are assigned to the UP phase. The Te:Mo ratio for the 2H-MoTe$_2$ component is calculated to be 2.03. After correction due to attenuation from the oxide overlayer the Te:Mo ratio is calculated to be 2.54. The Te:Mo ratio for the UP-MoTe$_x$ component in sample B is 2.12 and, when corrected for the oxide overlayer is 2.66. For sample C, there is a very small signal from 2H-MoTe$_2$ with Mo 3d$_{5/2}$ at 228 eV and the corresponding peak for Te 3d$_{5/2}$ at 572.7 eV. But the majority of the MoTe$_2$ peak intensity is from a new Mo 3d$_{5/2}$ peak at 227.5 eV and Te 3d$_{5/2}$ at 572.5 eV, which are assigned to chemical states associated with the UP phase of MoTe$_x$. The Te:Mo ratio corresponding to UP phase of MoTe$_2$ is 2.13 and, when corrected for the oxide overlayer is 2.72. The Te:Mo ratio for the 2H-MoTe$_2$ component is 2.04 and, when corrected for the oxide overlayer, is 2.61. It is key to note that in sample C the Mo 3d peak intensity associated with Mo oxide is much higher than that for MoTe$_2$, as well as the oxide intensity from the other samples. This suggests that, in spite of employing a large over pressure of uncracked Te (dimers) during growth, not only does Mo form predominantly the UP-MoTe$_x$ but that majority of Mo has an increased propensity for oxidation. This molybdenum oxide in sample C exhibits 2 different Mo oxidation states of +5 and +6. Reported peak position for 1T'-MoTe$_2$ for Mo 3d$_{5/2}$ is 227.7–228 eV and for Te 3d$_{5/2}$ is 572.1–572.6 eV [27,16]. The observed XPS peak from the phase assigned to UP-MoTe$_x$ for Te 3d$_{5/2}$ is consistent with the reported value but that for Mo 3d$_{5/2}$ is much lower that what has been reported for any Mo-Te bond and even metallic Mo 3d$_{5/2}$ at 227.8 eV [28]. It is also noted that in all 3 samples, the oxide peaks from Mo and Te in the O1s spectra could not be resolved because of the close proximity in electronegativity of Mo and Te [13]. The O 1s spectral feature also has
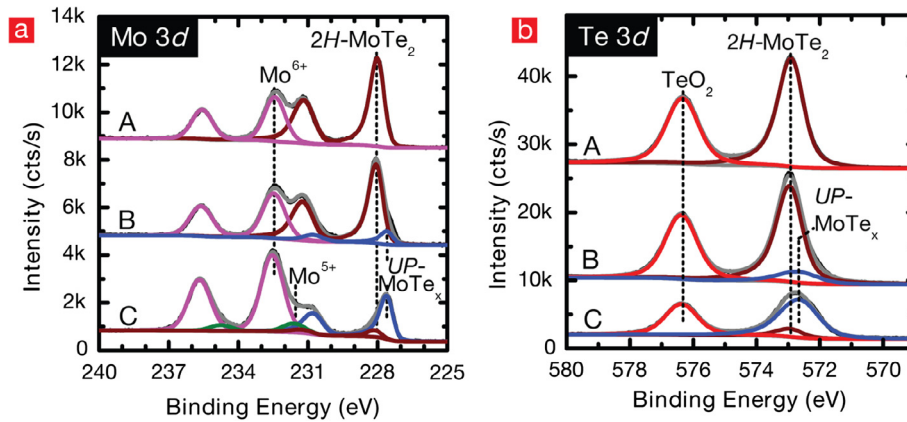
Fig. 3. (a) XPS on samples showing various phases and the extent of oxidation under different growth conditions. The pink line corresponds to Mo^{+6} oxide, maroon line to 2*H*-MoTe$_2$, blue line to *UP*-MoTe$_x$ (the unidentified phase), red line to TeO$_2$ and green line to Mo^{+5} oxide. (For interpretation of the references to colour in this figure legend, the reader is referred to the web version of this article.)

Table 3
XPS peak positions for Mo 3d$_{5/2}$ and Te 3d$_{5/2}$ as well as Te:Mo ratio corresponding to both phases 2*H*-MoTe$_2$ and *UP*-MoTe$_x$ compared to reported values.

Sample ID	Te:Mo flux ratio	Mo 3d$_{5/2}$ (eV)	Te 3d$_{5/2}$ (eV)	Te:Mo ratio w/o corr.	Te:Mo ratio corr.
Bulk 2*H*		227.8 (2*H*) (air exposed [14])	572.9 (2*H*) (air exposed [14])		2.03 (2*H*)
		228.0 (2*H*) (as cleaved [14])	573.0 (2*H*) (as cleaved [14])		
		227.8 (2*H*) (as cleaved [13])	572.4 (2*H*) (as cleaved [13])		
A	297	227.9 (2*H*)	572.8 (2*H*)		2.57 (2*H*)
B	98	227.9 (2*H*)	572.9 (2*H*)	2.03 (2*H*)	2.54 (2*H*)
		227.4 (*UP*)	572.6 (*UP*)	2.12 (*UP*)	2.66 (*UP*)
C	71	228 (2*H*)	572.9 (2*H*)	2.04 (2*H*)	2.61 (2*H*)
		227.5 (*UP*)	572.6 (*UP*)	2.13 (*UP*)	2.72 (*UP*)
1*T′*		227.7 (1*T′*) [27]	572.1 (1*T′*) [27]		
		228 (1*T′*) [16]	572.6 (1*T′*) [16]		

contributions from C-O and O-H. SI Fig. 4(a and b) shows that concentration of both molybdenum oxide and tellurium oxide concentrations are higher on the surface as seen from the increase in intensity of oxides at take-off angle of 45° as compared to 80°. (A take-off angle of 80° is much more bulk sensitive than 45°.) Also, the chemical bonding state of MoTe$_2$ is homogeneous through the analyzed depth, as the Mo-Te peak width remains constant when changing angle. Its worthy to note that the extent of oxidation in the telluride system is much more than previously reported MBE MoSe$_2$ [23].

3.3.2. Capped growth on GaAs substrate to study sensitivity to air exposure of MBE-MoTe$_2$

To understand the ease of oxidation of MoTe$_2$, on sample E, the Se cap was removed from Sample E by heating in a UHV system, followed by in situ XPS. After the initial XPS measurements, the sample was exposed to air for 20 min and then XPS done again. It is seen from SI Fig. 4(c–d) that oxide peaks appear in both Mo and Te XPS spectrum. Approximately, 8% of the surface area under goes oxidation in 20 min. The Se decapping is done in an oxide MBE system that is connected to LEED and XPS system to avoid air exposure. The O 1s signal observed in XPS (see SI Fig. 4(e)) prior to air exposure is likely due to physisorbed oxygen, post-decapping, from the oxide MBE chamber (base pressure of $\sim 1 \times 10^{-8}$ Torr). This is consistent with the fact that electronegativity difference between Mo and Te is 0.3 eV but that between O and Te is 1.4 eV, making the compound prone to oxidation [14,13]. Effect of air exposure in MBE grown films could be exacerbated by oxidation at the edges of MoTe$_2$ grains, similar to that reported for MBE grown WSe$_2$ films [29].

3.4. X-ray diffraction (XRD) and transmission electron microscopy (TEM)

3.4.1. MoTe$_2$ films on CaF$_2$ substrate

In order to get a better estimation of the inplane lattice constant of MBE 2*H*-MoTe$_2$ on CaF$_2$ as compared to the estimation using RHEED pattern, and to understand the preference of in-plane rotational orientation, grazing incidence X-ray diffraction (GI-XRD) was done. GI-XRD from sample A shows (see Fig. 4(a)) an extended line corresponding to overlapped $\{10\bar{1}0\}$ and $\{10\bar{1}1\}$ set of planes of MoTe$_2$ and the sharp high intensity peak is from the CaF$_2$ substrate. The in-plane lattice constant of 2*H*-MoTe$_2$ calculated from the $\{10\bar{1}0\}$ peak corresponds to 3.638 Å. The full width half maximum (FWHM) of 2*H*-MoTe$_2$ $\{10\bar{1}0\}$ peak is calculated to be $\sim$0.079 Å^{-1} and the direct beam FWHM is $\sim$0.009 Å^{-1}. By subtracting the width of the direct beam, the genuine FWHM of the $\{10\bar{1}0\}$ peak was estimated to be $\sim$0.07 Å^{-1} which translates to a grain size of $\sim$92 Å [30]. From Fig. 4(b), which is an inplane phi (ϕ) scan, we can see that MBE MoTe$_2$ undergoes significant twinning thus showing 2 sets of 6-fold symmetry diffraction patterns. The peak ratio between adjacent peaks separated by 30° is $\sim$0.5. This shows that almost 30% of the grains are twins. Also the wide FWHM (6.7–7.2°) of these peaks signifies a large deviation of grains from the preferred orientation. From measurements and simulation it has been shown in 2*H*-MoSe$_2$ that $\{10\bar{1}1\}$ and $\{10\bar{1}2\}$ peaks are $\sim$10 times weaker than $\{10\bar{1}3\}$ [31]. 2*H*-MoTe$_2$ having the same crystal structure as 2*H*-MoSe$_2$, we also observe the $\{10\bar{1}3\}$ set of peaks at higher q$_\perp$ (see SI Fig. 5(b)), from which the out of plane lattice constant (c-spacing) is calculated to be 14.4 Å. The c axis lattice constant obtained from cs-TEM as shown
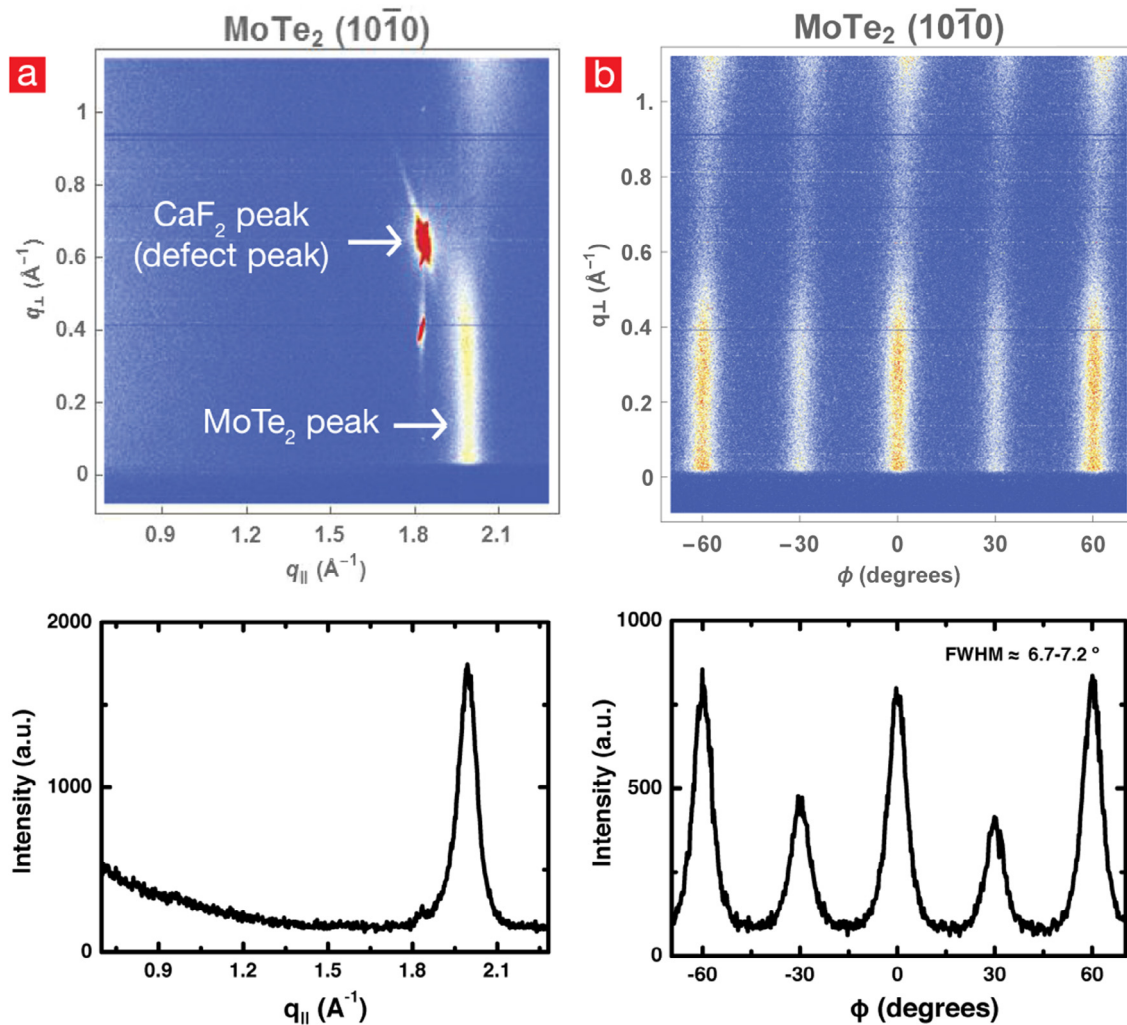
Fig. 4. For sample A (a) in-plane ω-2θ scan showing a peak corresponding to CaF_2 and $\{10\bar{1}0\}$ of $MoTe_2$. The extended streak in the perpendicular direction is due to overlap of the extended rods from $\{10\bar{1}0\}$ and $\{10\bar{1}1\}$ in reciprocal space due to the $\sim$5 monolayer thin film. Below it is the integrated intensity in a range of 0.02–0.15 Å^{-1} $q_\perp$ corresponding to $\{10\bar{1}0\}$ peak (b) The in-plane phi(ϕ) scan of the $\{10\bar{1}0\}$ peak of $MoTe_2$ to understand the rotational alignment and the extent of twinning in the grown film. Below it is the integrated intensity in a range of 0.02–0.15 Å^{-1} $q_\perp$.

in Fig. 5(b) is 13.9 Å. The reported value for the inplane lattice constant and c axis lattice constant from bulk $2H$-$MoTe_2$ are 3.52 Å and 13.966 Å, respectively [10]. To understand this discrepancy, we compare the intensity along $q_\perp$ (see SI Fig. 7 with simulations and observation for various polytypes of $NbSe_2$ by Toshihiro Shimada et al. [32] $2H$-$MoTe_2$ and $2H$-$NbSe_2$ share identical in-plane crystal structures and hence, would give similar intensity profiles along $q_\perp$ for various stacking orders (polytypes). Our $q_\perp$ (see SI Fig. 7 scan closely matches the one reported by Toshihiro Shimada et al. [32] on Se-GaAs, which is explained as a combination of $2Hb$ and $3R$ NbSe_2. $2Hb$ and $3R$ both have the trigonal prismatic monolayer but the stacking sequence is different, with $3R$ having a 3-layer periodicity as compared to 2-layer for $2Hb$. The value for MBE $2H$-$MoTe_2$ obtained by TEM is spatially local but X-ray beam for GI-XRD has a foot print of $\sim$2 mm $\times$ 10 mm.

Both, the excess Te ($>$2 Te:Mo film stoichiometry) measured using XPS and the presence of stacking faults resulting in mixture of $2Hb$ and $3R$ phases could be the contributing factors for the observed larger 'a' and 'c' lattice constants in MBE $2H$-$MoTe_2$ compared to bulk $2H$-$MoTe_2$.

SI Fig. 6(b) shows the cs-TEM of the mixed phase sample B. Comparing the film thickness for sample A and sample B (see SI Fig. 6(a and b)), they are very similar but apart from lattice spacing,

phase composition from sample B is not discernible. $1T'$- $MoTe_2$ is known to crystallize in $P2_1/m$ space group with lattice constants of a = 6.33 Å, b = 3.48 Å and c = 13.82 Å [10], where b is very close to the lattice constant of $2H$-$MoTe_2$. Therefore, for the sample C since the RHEED shows polycrystalline rings, irrespective of the in-plane rotational orientation of the film, if it was purely $1T'$, we would expect to observe a ring corresponding to the $\{010\}$ set of planes in a similar scan as for Sample A (Fig. 4(a) or SI Fig. 5(a)). SI Fig. 5(c) shows the GI-XRD on sample C ie. UP-$MoTe_x$. SI Fig. 5(c) shows that there is no signal observed corresponding to $1T'$-$MoTe_2$, the only peak is corresponding to CaF_2. This is likely due to extremely low signal from the polycrystalline highly defective $1T'$-$MoTe_2$ thin film or the film has a new unknown phase with a different crystal structure. Finally, the GI-XRD exercise also shows the variability in crystallinity of CaF_2 from substrate to substrate, motivating the use of epi-ready substrates such as, GaAs.

3.4.2. MoTe₂ films on GaAs substrate

It is very interesting to note that after cooling to room temperature, although the films on CaF_2 (Fig. 5(a)) only show $\sim$10 nm droplet like structures that are $\sim$4–5 nm high, sample D shows 100s nm long Te crystallites on the surface. The height of these crystallites is $\sim$9 nm and they are about $\sim$50 nm wide. From AFM image
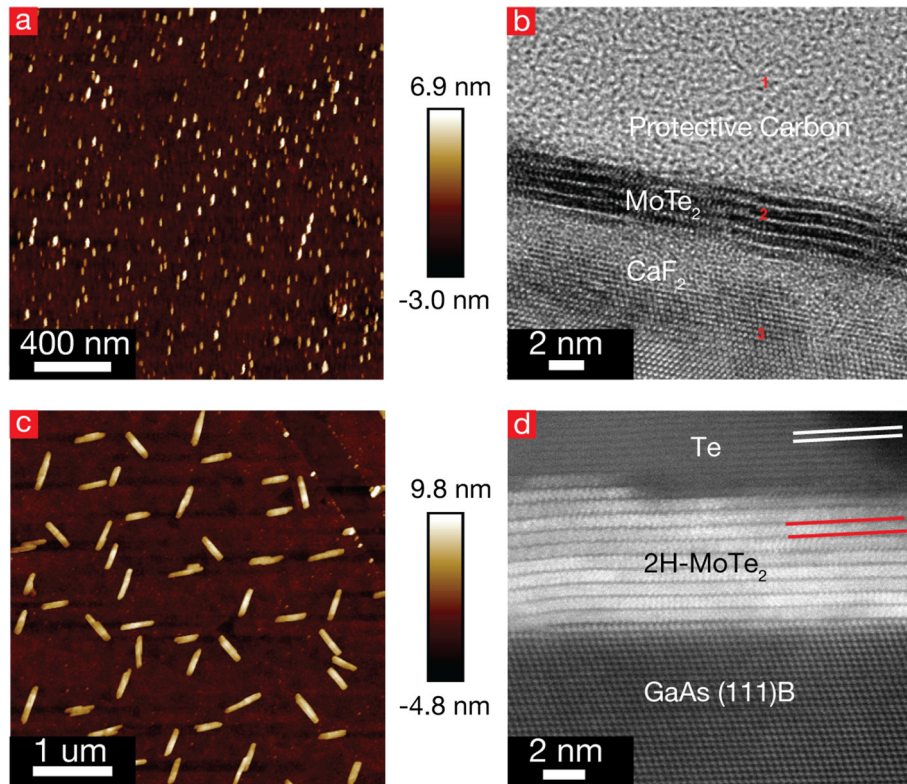
Fig. 5. Sample A: (a) The surface of the thin film post-growth on sample A and (b) cs-TEM of $2H$-MoTe$_2$ on CaF$_2$. Sample D: (c) The surface of the thin film of $2H$-MoTe$_2$ on GaAs post-growth shows several tellurium crystallites, surprisingly with preferential direction of orientation. (d) cross-sectional TEM shows the abrupt interface between GaAs and MoTe$_2$, better quality of ~9 monolayer MoTe$_2$ than on CaF$_2$ and pure tellurium crystallite with a significantly different lattice constant and contrast. The pair of white lines and the pair of red lines are a guide to the eye marking the difference in lattice constant of Te and $2H$-MoTe$_2$.

(Fig. 5(c)) and SEM image (SI Fig. 8(a)) we can observe that these crystallites have preferential crystallographic orientation with the underlying GaAs (1 1 1) with triangular symmetry. The fact that these crystallites are purely tellurium is confirmed by the markedly distinct lattice spacing compared to MoTe$_2$ as seen in the high resolution transmission electron microscopy (HRTEM) image shown in Fig. 5(d). This is further confirmed by TEM Energy-dispersive X-ray spectroscopy (not shown). The HRTEM image (Fig. 5(d)) also shows a high quality of MoTe$_2$ with a c-axis lattice spacing of 13.9 Å consistent with $2H$-MoTe$_2$. These crystallites could have likely been formed during the cooling process to room temperature. We don't observe such Te crystallite formation on films on CaF$_2$ (see SI Fig. 3(a)). XRD scan in SI Fig. 8(b) shows that at room temperature the (0 0 4) peak for sample D appears at 24.46°, which is lower than that for bulk $2H$-MoTe$_2$ and $1T'$-MoTe$_2$ [10]. It corresponds to a c-spacing of 14.52 ± 0.05 Å. It is analyzed below along with (0 0 4) peak of sample E (see Table 4).

From the phase diagram [9], one might expect mixed phase formation during the post-growth anneal at 550 °C under Te. LEED and XRD was done to check the phase of the film grown. Prior to LEED, the Se cap was desorbed by annealing the sample in UHV at 300 °C for ~30 min. A LEED pattern measured with 40 eV electrons (Fig. 6(a) shows two sets of spots with the outer hexagonal pattern corresponding to the lattice constant of $2H$-MoTe$_2$ ('a' lattice constant using LEED = 3.57 ± 0.03 Å) and the inner pattern corresponding to an effective 2×2 superstructure. This is very interesting because it is consistent with the second set of RHEED streaks seen for sample D in Fig. 1(e–f), discussed previously. One possible explanation for the extra spots is a change in the surface periodicity relative to the bulk $2H$-MoTe$_2$ crystal structure due to a reconstruction or the presence of ordered defects. An alternate possibility is that the large electron spot size (~1 mm) may be averaging over three domains of $1T'$-MoTe$_2$ rotated by 60 degrees and 120 degrees (see SI Fig. 9).

Table 4
In-plane and out of plane lattice constants for the $2H$-MoTe$_2$ samples in this study obtained by various techniques.

Sample ID	RHEED (Å)	XRD (Å)	GI-XRD (Å)	LEED (Å)	TEM (Å)
A	a = 3.5 ± 0.1		a = 3.64 ± 0.03		c = 13.9 ± 0.1
			c = 14.4 ± 0.03		
D	a = 3.6 ± 0.05	c = 14.52 ± 0.05			c = 13.8 ± 0.1
E	a = 3.5 ± 0.1	c = 14.25 ± 0.04		a = 3.57 ± 0.03	
Bulk 2H		a = 3.52085 [10]			
		c = 13.9664 [10]			
Bulk 1T'		a = 6.3274 [10]			
		b = 3.4755 [10]			
		c = 13.8100 [10]			
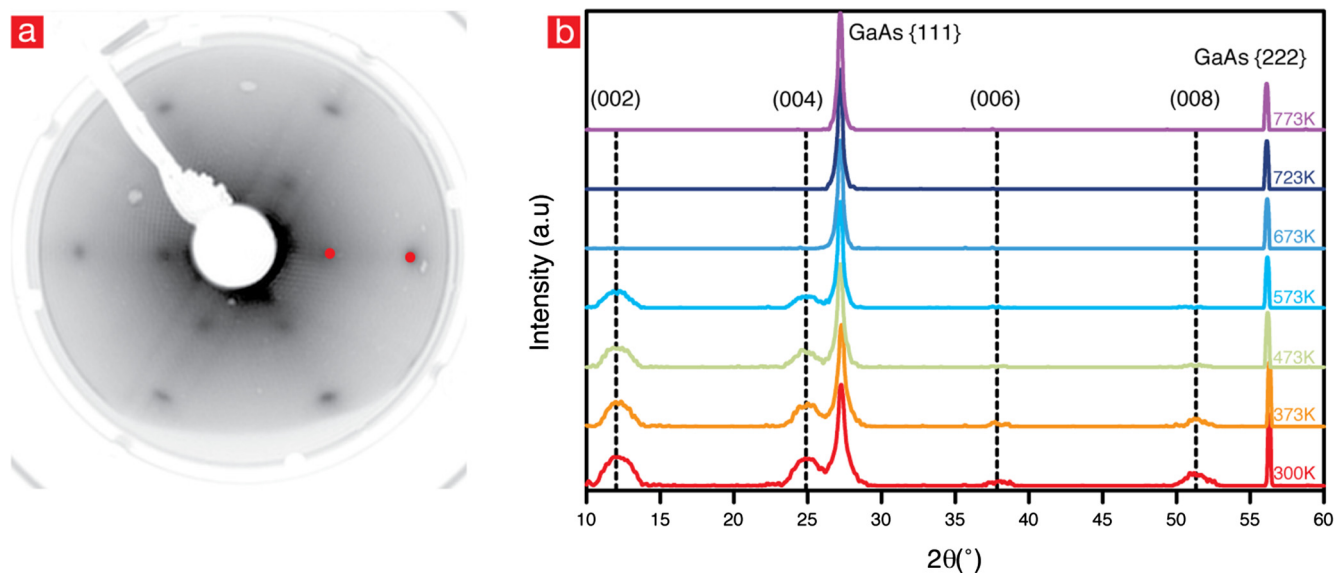
Fig. 6. (a) LEED from sample E post-decapping without any air exposure, the red spots are guide to the eye demonstrating the 2×2 superstructure (b) Temperature dependent XRD on sample E under nitrogen environment showing the phase of $MoTe_2$ and its thermal stability.

To distinguish between these possibilities, temperature dependent XRD was done on sample E. At room temperature (002), (004), (006) and (008) peak 2θ positions of the as grown film are 12.17°, 25.02°, 38.02° and 51.38° respectively. The reported room temperature 2θ positions for the (002), (004), (006) and (008) peaks for $2H$-$MoTe_2$ are 12.66°, 25.48°, 38.63° and 52.34° respectively. Keum et al. [10] report using temperature dependent XRD that the (004) 2θ peak of $2H$-$MoTe_2$ is at 25.5° at room temperature and it shifts to slightly greater than 26° at temperatures above 600 °C corresponding to (004) 2θ peak of $1T'$-$MoTe_2$. In our case, the (004) 2θ peak position is much lower than both peaks ($\sim$0.5° lower than $2H$-$MoTe_2$), which corresponds to a c-spacing of 14.25 ± 0.04 Å, and the peaks from the film is lost above 400 °C. Therefore, without a chalcogen over pressure, MBE grown few-layer $2H$-$MoTe_2$ dissociates between 400 °C and 500 °C (see Fig. 6 (b)). Also, sample D (see SI Fig. 8(b)) which was grown without anneal at 550 °C anneal has $\sim$0.5° lower than sample E. Peak at smaller 2θ implies larger lattice constant but its origin is unclear yet. One possible explanation is the presence of excess tellurium in the crystal, which has been previously reported for bulk crystals [31]. The $MoTe_2$ phase diagram [9] shows that $2H$-$MoTe_2$ is not a line compound. The $2H$ phase of $MoTe_2$ can be formed in spite of a 1% sub- or super-stoichiometric incorporation of tellurium. Hence, as XRD for both samples on GaAs does not show detectable peaks from the $1T'$-$MoTe_2$ phase, the 2×2 superstructure observed in LEED, is likely a surface feature rather than the presence of rotated domains of $1T'$-$MoTe_2$. Lattice constants obtained from the various techniques described above have been tabulated in Table 4.

3.5. Electrical measurements

Sheet resistivity of the sample A and sample C were measured to be 5468 Ω/□ and 13,255 Ω/□, respectively. This is of interest because film on sample A is $2H$-$MoTe_2$ and film on sample C is assigned to UP-$MoTe_x$. $1T'$-$MoTe_2$ is metallic and is expected to have lower resistance than $2H$-$MoTe_2$. From XPS of sample C, we observe that more Mo is oxidized than that is bound to Te, so, weather UP phase is highly defective $1T'$-$MoTe_2$ or a new unknown phase, this extensive oxidation could be the cause of the significant increase in resistivity. TeO_2 glasses show semiconducting behavior [33].

In order to test the electrical characteristic of the transferred MBE grown $MoTe_2$ film on GaAs, contacts were made to the transferred flake on SiO_2 (SI Fig. 10(a)). Using backgating, no modulation was observed (see SI Fig. 10(b and c)). Excess Te in the film could a cause for this behavior. But even if techniques are devised to overcome excess Te incorporation, its important to note that using XPS, oxidation of 8% of the surface area in 20 min was observed and, through the process of exfoliation and fabrication the film is likely to undergo extensive oxidation if appropriate capping is not done.

4. Conclusion

This work employs extensive large area structural and chemical characterizations of MBE grown few layer $MoTe_2$, with complementing electrical characterization. We show that for growth of few layer $2H$-$MoTe_2$ at a low temperature of 340 °C and growth rate of $\sim$6 min/ML, we need an incident Te:Mo flux greater than 100. The $2H$ phase growth on CaF_2 and GaAs is confirmed using RHEED, Raman and XPS, but the Te:Mo stoichiometry determined by XPS. GI-XRD shows a small grain size of $\sim$90 Å, twinning and a higher-than-expected 'a' and 'c' spacing for MBE $2H$-$MoTe_2$ on CaF_2. XRD on MBE $2H$-$MoTe_2$ on GaAs also shows larger c spacing than both bulk $2H$-$MoTe_2$ and bulk $1T'$-$MoTe_2$. On CaF_2, greater than 2 Te:Mo stoichiometry determined by XPS and on GaAs, Te crystallite formation on the surface, and a 2×2 pattern in RHEED and LEED have been observed. All these have been hypothesized as signs of excess Te incorporation into few-layer $2H$-$MoTe_2$ during growth using elemental Mo and uncracked Te sources. At ambient pressure in N_2 atmosphere, MBE $2H$-$MoTe_2$ on GaAs is only stable up to 300 °C. Excess Te in the film can explain the high electrical conductivity, non-modulating behavior and easy dissociation of the film with increasing temperature prior to phase transition to the $1T'$ phase, a more stable phase at higher temperatures. Finally, we demonstrate the swift oxidation ($\sim$8% surface area in 20 min) of the MBE $MoTe_2$ film on exposure to air. With the various complementing large area and local characterizations, this study has provided insight into the few layer MBE growth of Mo-Te system on 3D substrates. We believe our work motivates study into new phases obtained under UHV conditions as well as into techniques to directly probe and overcome excess Te incorporation.

5. Experimental methods

5.0.1. Raman spectroscopy

Raman measurements were performed in the backscattering configuration using a WITec Alpha 300 system at room temperature. Measurement was done using a $100\times$ objective, 1800 grooves/mm grating, 488 nm laser and 0.75 mW power.

5.0.2. X-ray photoelectron spectroscopy

XPS on the CaF_2 samples was carried out ex-situ using a monochromated Al Kα source (hν = 1486.7 eV) and an Omicron Argus detector (MCD-128) operating with a pass energy of 15 eV. XPS spectra were acquired at a pass energy of 15 eV and take-off angle (defined with respect to the sample surface) of $45°$ and $80°$. For XPS peak deconvolution, the spectral analysis software Aanalyzer was employed, where Voigt line shapes and an active Shirley background were used for peak fitting [34].

XPS on the $2H$-$MoTe_2$/n$^+$GaAs samples was measured using a non-monochromated Al Kα source and a Scienta R4000 electron analyzer operating at a pass energy of 100 eV. All spectra were measured at normal emission, i.e. 90 degrees relative to the sample surface. Central peak locations were determined by Lorentzian fits with linear backgrounds.

5.0.3. X-ray diffraction

Out of plane XRD and temperature dependent XRD on the $2H$-$MoTe_2$/GaAs samples is done using the Rigaku SmartLab X-ray Diffractometer with Cu Kα X-ray source. The GI-XRD is done using the G2 hutch at the CHESS beamline (http://www.chess.cornell.edu/gline/G2.htm), operating with a X-ray energy of 11.31 keV.

5.0.4. Transmission electron microscopy

The atomic structure analysis for sample A and sample D was carried out on FEI Titan 80–300 Transmission Electron Microscope operated at 300 kV.

TEM on sample B was done using JOEL ARM200F atomic resolution analytical microscope.

5.0.5. LEED

LEED on the $2H$-$MoTe_2$/n$^+$GaAs samples was measured using a Specs ErLEED 3000 system with an incident electron energy of 40 eV. The electron spot size was approximately 1 mm in diameter, and the total angular field of view was 100 degrees. Following the Se decapping at $300\,°C$, in situ LEED and XPS measurements were both performed at room temperature in an analysis chamber with pressure below $\sim1 \times 10^{-10}$ Torr.

Appendix A. Supplementary material

Supplementary data associated with this article can be found, in the online version, at https://doi.org/10.1016/j.jcrysgro.2017.10.024.

References

[1] K. Deng et al., Nat. Phys. 12 (2016) 1105–1111.
[2] C. Gong, H. Zhang, W. Wang, L. Colombo, R.M. Wallace, K. Cho, Appl. Phys. Lett. 103 (2013) 053513.
[3] H.C. Diaz, Y. Ma, R. Chaghi, M. Batzill, Appl. Phys. Lett. 108 (2016) 191606.
[4] J. Chen, G. Wang, Y. Tang, J. Xu, X. Dai, J. Jia, W. Ho, M. Xie, 2016. Available from: arXiv preprint <arXiv:1612.06105>.
[5] R. Schlaf, O. Lang, C. Pettenkofer, W. Jaegermann, J. Appl. Phys. 85 (1999) 2732–2753.
[6] R. Yan, S. Fathipour, Y. Han, B. Song, S. Xiao, M. Li, N. Ma, V. Protasenko, D.A. Muller, D. Jena, H.G. Xing, Nano Lett. 15 (2015) 5791–5798.
[7] M.O. Li, D. Esseni, J.J. Nahas, D. Jena, H.G. Xing, IEEE J. Electron Dev. Soc. 3 (2015) 200–207.
[8] M.O. Li, D. Esseni, D. Jena, H.G. Xing, Lateral transport in two-dimensional heterojunction interlayer tunneling field effect transistor (Thin-TFET), in: Device Research Conference (DRC), 2014 72nd Annual, 2014, pp. 17–18.
[9] L. Brewer, R. Lamoreaux, Binary Alloy Phase Diagrams, second ed., Ed. T.B. Massalski, ASM International, Materials Park, Ohio, vol. 3, 1990, pp. 2675–2676.
[10] D.H. Keum, S. Cho, J.H. Kim, D.-H. Choe, H.-J. Sung, M. Kan, H. Kang, J.-Y. Hwang, S.W. Kim, H. Yang, K.J. Chang, Y.H. Lee, Nat. Phys. 11 (2015) 482–486.
[11] Y. Yu, G. Wang, S. Qin, N. Wu, Z. Wang, K. He, X.-A. Zhang, Carbon 115 (2017) 526–531.
[12] S. Cho, S. Kim, J.H. Kim, J. Zhao, J. Seok, D.H. Keum, J. Baik, D.-H. Choe, K. Chang, K. Suenaga, S.W. Kim, Y.H. Lee, H. Yang, Science 349 (2015) 625–628.
[13] J. Bernede, C. Amory, L. Assmann, M. Spiesser, Appl. Surface Sci. 219 (2003) 238–248.
[14] W. Jaegermann, D. Schmeisser, Surface Sci. 165 (1986) 143–160.
[15] F. Gamble, J. Solid State Chem. 9 (1974) 358–367.
[16] L. Zhou, K. Xu, A. Zubair, A.D. Liao, W. Fang, F. Ouyang, Y.-H. Lee, K. Ueno, R. Saito, T. Palacios, J. Kong, M.S. Dresselhaus, J. Am. Chem. Soc. 137 (2015) 11892–11895.
[17] J.C. Park, S.J. Yun, H. Kim, J.-H. Park, S.H. Chae, S.-J. An, J.-G. Kim, S.M. Kim, K.K. Kim, Y.H. Lee, ACS Nano 9 (2015) 6548–6554.
[18] J. Zhou et al., Adv. Mater. 1603471 (1–8) (2017).
[19] J. Bernede, M. Kettaf, A. Khelil, M. Spiesser, Phys. Status Solidi (A) 157 (1996) 205–209.
[20] H. Zhu, Q. Wang, C. Zhang, R. Addou, K. Cho, R.M. Wallace, M.J. Kim, Adv. Mater. (2017).
[21] S. Vishwanath, X. Liu, S. Rouvimov, L. Basile, N. Lu, A. Azcatl, K. Magno, R.M. Wallace, M. Kim, J.-C. Idrobo, J.K. Furdyna, D. Jena, H.G. Xing, J. Mater. Res. 31 (2016) 900–910.
[22] A. Roy, H.C. Movva, B. Satpati, K. Kim, R. Dey, A. Rai, T. Pramanik, S. Guchhait, E. Tutuc, S.K. Banerjee, ACS Appl. Mater. Interf. 8 (2016) 7396–7402.
[23] S. Vishwanath, X. Liu, S. Rouvimov, P.C. Mende, A. Azcatl, S. McDonnell, R.M. Wallace, R.M. Feenstra, J.K. Furdyna, D. Jena, H.G. Xing, 2D Materials 2 (2015) 024007.
[24] A. Koma, K. Saiki, Y. Sato, Appl. Surface Sci. 41 (1990) 451–456.
[25] C. Adenis, V. Langer, O. Lindqvist, Acta Crystallogr. Sect. C: Cryst. Struct. Commun. 45 (1989) 941–942.
[26] A. Pine, G. Dresselhaus, Phys. Rev. B 4 (1971) 356.
[27] C.H. Naylor, W.M. Parkin, J. Ping, Z. Gao, Y.R. Zhou, Y. Kim, F. Streller, R.W. Carpick, A.M. Rappe, M. Drndic, J.M. Kikkawa, A.T.C. Johnson, Nano Lett. 16 (2016) 4297–4304.
[28] F. Werfel, E. Minni, J. Phys. C: Solid State Phys. 16 (1983) 6091.
[29] J.H. Park, S. Vishwanath, X. Liu, H. Zhou, S.M. Eichfeld, S.K. Fullerton-Shirey, J.A. Robinson, R.M. Feenstra, J. Furdyna, D. Jena, H.G. Xing, ACS Nano 10 (2016) 4258–4267.
[30] T. Shimada, H. Nishikawa, A. Koma, Y. Furukawa, E. Arakawa, K. Takeshita, T.-I. Matsushita, Surface Sci. 369 (1996) 379–384.
[31] P. James, M. Lavik, Acta Crystallogr. 16 (1963), 1183-1183.
[32] T. Shimada, Y. Furukawa, E. Arakawa, K. Takeshita, T. Matsushita, H. Yamamoto, A. Koma, Solid State Commun. 89 (1994) 583–586.
[33] R. Hampton, W. Hong, G. Saunders, R. El-Mallawany, J. Non-crystalline Solids 94 (1987) 307–314.
[34] A. Herrera-Gomez, A. Hegedus, P. Meissner, Appl. Phys. Lett. 81 (2002) 1014–1016.